PLANETARY SCIENCE

Modern water at low latitudes on Mars: Potential evidence from dune surfaces

Xiaoguang Qin[1]†*, Xin Ren[2]†*, Xu Wang[1]†*, Jianjun Liu[2]†*, Haibin Wu[1,3], Xingguo Zeng[2], Yong Sun[4], Zhaopeng Chen[2], Shihao Zhang[1], Yizhong Zhang[2], Wangli Chen[2], Bin Liu[2], Dawei Liu[2], Lin Guo[2], Kangkang Li[1], Xiangzhao Zeng[2], Hai Huang[2], Qing Zhang[2], Songzheng Yu[2], Chunlai Li[2], Zhengtang Guo[1]

Landforms on the Martian surface are critical to understanding the nature of surface processes in the recent past. However, modern hydroclimatic conditions on Mars remain enigmatic, as explanations for the formation of observed landforms are ambiguous. We report crusts, cracks, aggregates, and bright polygonal ridges on the surfaces of hydrated salt-rich dunes of southern Utopia Planitia (~25°N) from in situ exploration by the Zhurong rover. These surface features were inferred to form after 1.4 to 0.4 million years ago. Wind and CO_2 frost processes can be ruled out as potential mechanisms. Instead, involvement of saline water from thawed frost/snow is the most likely cause. This discovery sheds light on more humid conditions of the modern Martian climate and provides critical clues to future exploration missions searching for signs of extant life, particularly at low latitudes with comparatively warmer, more amenable surface temperatures.

INTRODUCTION

Does liquid water recently exist on the contemporary surface of Mars? This question is critical for understanding the recent climatic evolution of the polar ice caps, the habitable environment, and even the potential for life on Mars (1). Previous studies show that abundant liquid water existed on early Mars (2–7). However, as the early atmosphere has disappeared, the climate and environment on Mars have undergone substantial changes (8), with the resultant temperature and pressure conditions becoming unfavorable for the stability of liquid water on Mars today (9, 10).

Nevertheless, the observed liquid drops on the robotic arms of the Phoenix rover indicate that conditions allowing for the existence of liquid saline water emerge at high-latitude regions of Mars in summer because the thermodynamics of freeze-thaw cycles can lead to the formation of saline solutions with freezing temperatures lower than current summer ground temperatures (11). In contrast, indirect evidence for modern hydrological activity above ground including recurring slope lineae (12) and gullies (13) remains under debate. For example, some conflicting scenarios such as dry versus wet mechanisms have been proposed for their formation (14, 15). The main argument against the wet hypothesis lies in the inadequate amount of water required to trigger such large-scale (i.e., at least several hundred meters long) slope flows (14). Numerical modeling (16) suggests that suitable climatic conditions for liquid water can occur on present-day Mars. If this projection is right, then there may be small amounts of surface water hidden from view. In this case, studies on small-scale (i.e., <1 m) surface features on a diversity of landscapes are therefore essential to depict a complete picture of contemporary hydrological processes on Mars. In particular, surface morphological features of sand dunes at low latitudes are rarely investigated, which hampers our understanding of hydroclimatic variations in the region where the comparatively mild ground temperatures may support life.

On 15 May 2021, Zhurong rover landed in southern Utopia Planitia (25.066°N, 109.925°E; −4,099.4 m above the Mars Orbiter Laser Altimeter geoid) in the northern hemisphere of Mars, which belongs to the Late Hesperian northern lowlands (17). For 9 months, a comprehensive exploration of the landing site and its environment has been conducted using the Navigation and Terrain Camera (NaTeCam), the Multispectral Camera (MSCam), and the Mars Surface Composition Detector (MarSCoDe) aboard Zhurong rover (18). By studying the surficial microstructure, morphology, and chemical compositions of dunes, our investigation provides critical insights into the possibility of water activity at low latitudes during the contemporary period on Mars.

RESULTS

Dune landform

Barchan dunes with a crescent shape morphology, as one type of transverse aeolian ridge (TAR), are sparsely distributed at the Zhurong landing site (Fig. 1A). They are completely isolated from each other and exhibit a bright color (high albedo) in high-resolution image camera (HiRIC) pictures of 0.7-m ground pixel size taken by the Tianwen-1 orbiter (Fig. 1A). As the rover advanced southward in the first 4 months, four dunes (designated Dunes 1, 2, 3, and 4) were investigated in situ.

Two types of sands with high and low albedos were discovered on the ground. The dark sands always overlie the bright dunes (Fig. 1B), implying two generations of sand dunes. The bright type is the early barchan dune, 15 to 30 m in length and 3 to 10 m in width (Fig. 1E). The dark type, having a similar color as the surrounding soils (Fig. 1, B, D, and E), comes in several forms of a small-sized longitudinal dune, a sand ridge, or sand particles
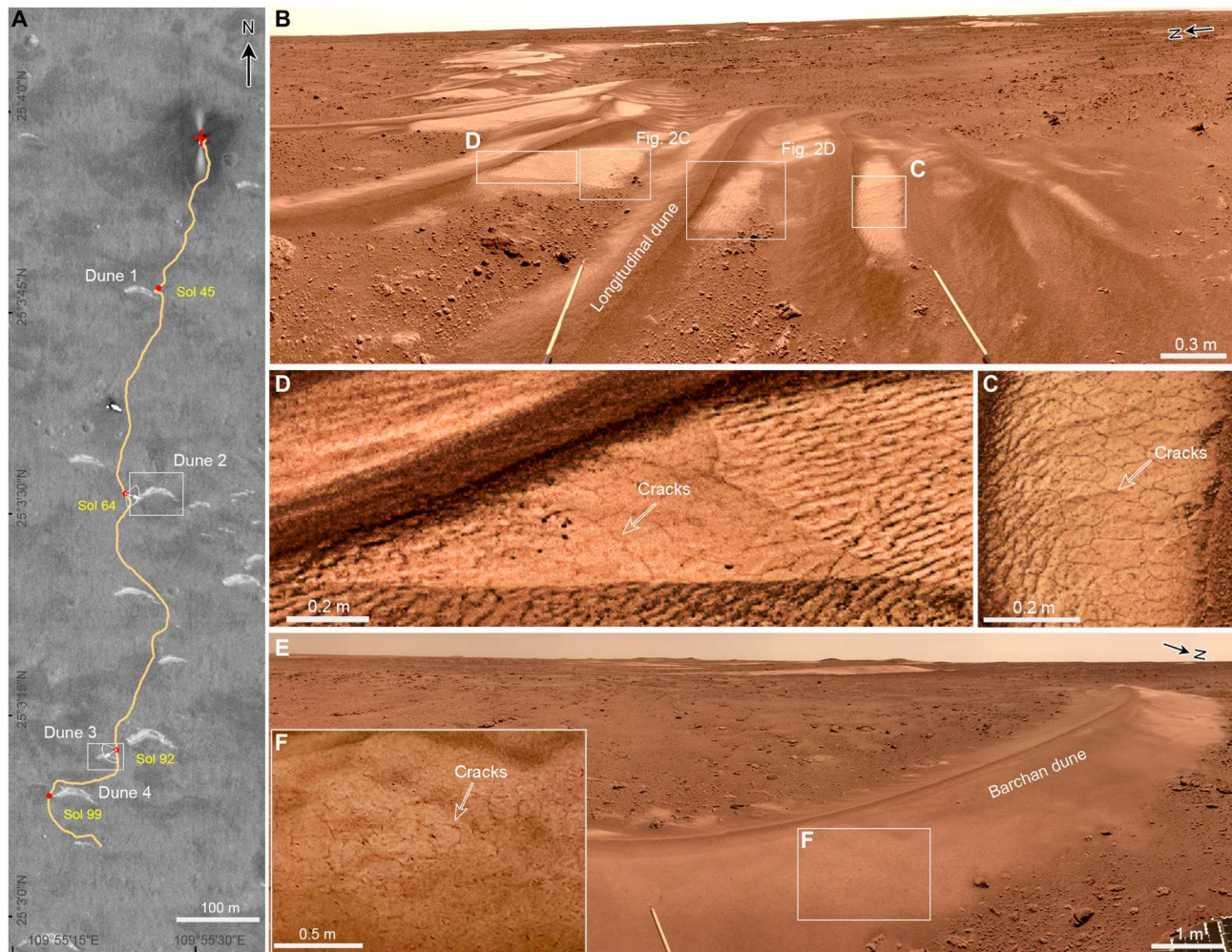
Fig. 1. Exploration route of Zhurong rover and cracks on bright sand dunes. (**A**) Map of the exploration route of Zhurong from May to September 2021. The HiRIC photo (0.7-m resolution) was taken by the Tianwen-1 orbiter. Dunes 1 to 4, marked by white rectangles, were measured in situ on Sols 45, 64, 92, and 99, respectively. (**B**) Panorama mosaics acquired by NaTeCam of longitudinal dunes on barchan Dune 2, with white rectangles indicating positions of the cracks. (**C** and **D**) Cracks developed on the southwestern slope of longitudinal dune on the western wing of Dune 2, with a white arrow pointing to one of the cracks. (**E**) Panorama mosaics acquired by NaTeCam of barchan Dune 3, with white rectangles indicating positions of the cracks. (**F**) Cracks on the northern slope of Dune 3. Credit: CNSA/GRAS.

coated on the surface of bright barchan dunes, of which the northwestward longitudinal dunes overlying the west flank of the bright barchan dune are the most typical form (Fig. 1B). Continuous transitional depositional patterns were observed from sands on surficial soils to the dark longitudinal dunes (Fig. 1B). The observations suggest that the dark sand dunes were later than bright barchans and formed most recently, probably in the modern environment.

Crusts, agglomerated particles on dune surfaces, and the composition

Pictures taken by the MSCam and the microscopic camera show that different forms of cementation exist on dune surfaces, with a crust developed on the bright dunes (Fig. 2B and fig. S1, B and E) and agglomerated particles (granules/aggregation) on the dark dunes (Fig. 2B and fig. S1, C and E). These structures arise from the cementation of fine and medium sand grains. These agglomerates (~3 to 15 mm) were turned into fine and medium sand grains (0.1 to 0.3 mm) using the laser-induced breakdown spectrometer

(LIBS; fig. S2C). By comparing the short-wave infrared passive spectra (SWIR) data to the standard mineral spectrum database, we confirm that there are hydrated sulfates, hydrated silica (especially Opal-CT), trivalent iron oxide minerals (especially ferrihydrite), and possibly chlorides in the sands (figs. S3 and S4). Inorganic cements such as hydrated sulfates and hydrated silica/ferric substances are therefore the most likely materials for cementing sand grains to form the crusts and agglomerated particles.

Compositional element data obtained using LIBS (fig. S5 and table S1) show that bright and dark sands are characterized by high Fe and Mg contents. Silica makes up ~52 to 56% over ~85 to 90% of total silicate oxides, which makes it more abundant than in any basaltic phases. As seen from the total percentage of oxides (table S1), undetectable material accounts for ~15 and ~10 wt % of bright and dark sands, respectively. Previous studies have shown that components undetectable by LIBS include all volatiles, i.e., S, Cl, and P from some salts (7) and H or OH^- from hydrated
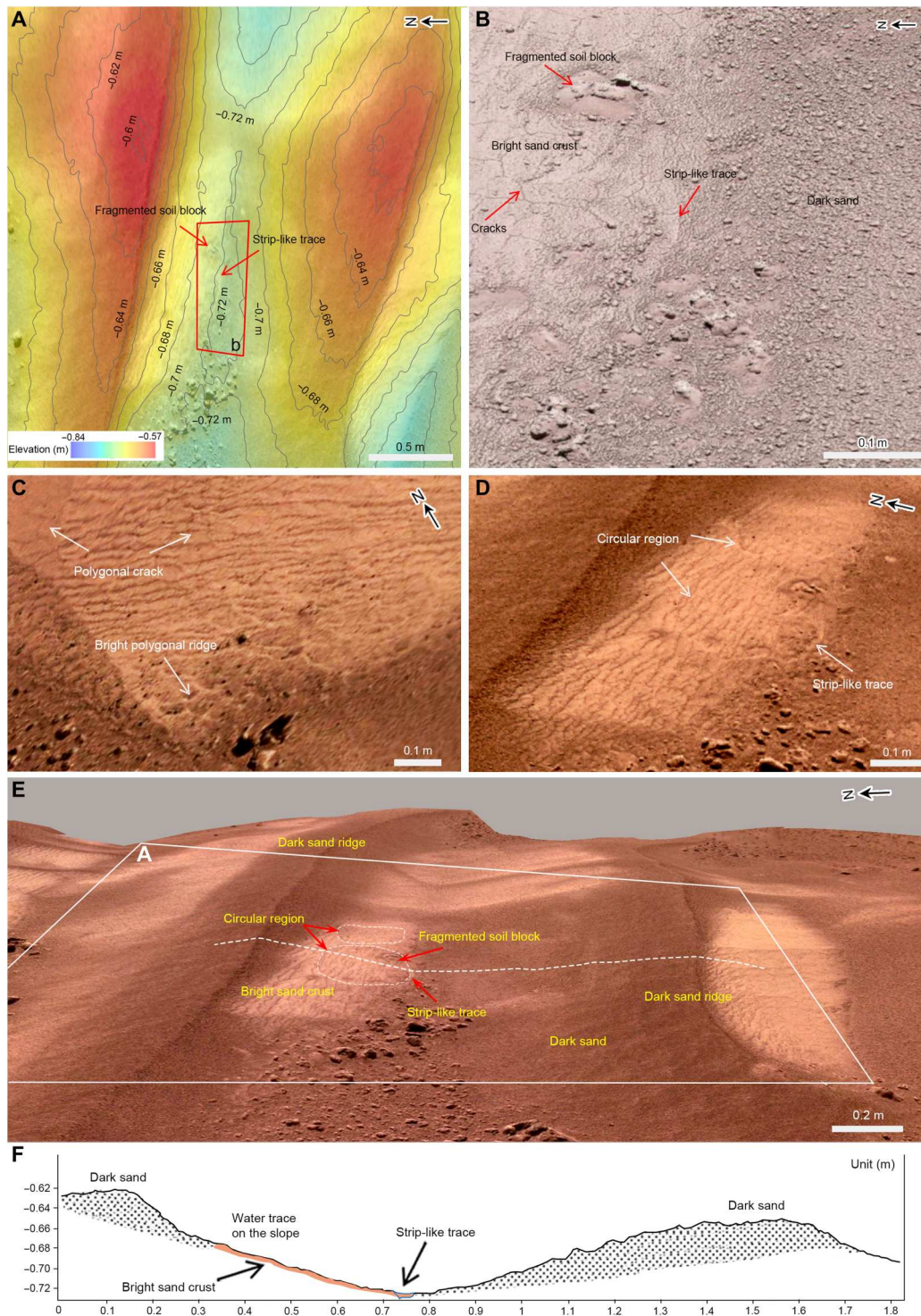
Fig. 2. Water traces on bright sand dunes. (**A**) Topographic contour map of the environs where the trace is located. The coordinate system is east-north-up local Cartesian coordinate, and the origin is that of the rover coordinate system. The background digital orthophoto map photo was taken by NaTeCam. (**B**) MSCam bird's-eye-view photo showing a strip-like trace and a likely water-soaked fragmented soil block. (**C**) Enlarged photo showing polygonal cracks and bright polygonal ridges. (**D**) Enlarged photo showing circular region with the strip-like trace as a part. (**E**) NaTeCam three-dimensional image of an interdune depression between two dark longitudinal dunes. (**F**) A cross section of the dune along the profile of the white dash line in (E). Credit: CNSA/GRAS.

phases (i.e., ferric hydroxides) and amorphous phases (i.e., more crystalline hydrated silica).

Cracks on dune surfaces

Polygonal cracks are ubiquitous in Dunes 2 and 3. They are developed on the surfaces (Fig. 1, D and F) of bright barchan dunes. The surfaces of dark sands without encrustation are mainly dotted with agglomerated particles (fig. S1, C and E), therefore cracks are rarely seen. Statistically, the crack polygons have an average area of 55.2 cm^2 and an average side length of 4.8 cm (fig. S7), belonging to the smaller fracture type than the cracks previously observed by remote sensing (19). Calculated according to a depth-to-width ratio of a polygonal fracture between 1/3 and 1/4 (20), the thickness of the crust could be 1.25 to 1.7 cm. The crack polygons form triangular to heptagonal shapes in plan view, with a dominance of pentagonal shapes. The internal angles of the polygons average around 110°, and most cracks have Y-shaped intersections.

Other related features

On the interdune depression of Dune 2, MSCam captured a light-toned strip-like trace >40 cm long and ~1.5 cm wide (i.e., much brighter than surrounding area; Fig. 2B). The centimeter-scale-resolution and three-dimensional reconstructed image of the dune using NaTeCam stereoscopic images shows that this strip-like trace lies along the lowest trough line of the depression and extends along strike of the depression to separate the bright and dark sands (Fig. 2E). On the right (south) side of the trace, there is a dark sand–covered slope (angle = 4.3°; length = 0.93 m). On the left (north) side lies an encrusted bright sand slope (angle = 7.2°; length = 0.42 m) with abundant polygonal cracks, where there are two faint circular regions (Fig. 2, D and E). The strip-like trace is the right edge of a circular (diameter, ~30 cm; Fig. 2, D and E). This topographic structure would allow water, if the amount of stably existing water is enough and surficial crust is hard to penetrate, to collect at the lowest part of depression from the bright sand crust on the left (Fig. 2F).

In addition, there is a fragmented block of soil on the bright sand crust beside the strip-like trace (Fig. 2B). The soil block is surrounded by a pile of well-distributed fine detritus. In the lowest part of another interdune depression of Dune 2, some polygonal bright lines occur in the dark sand thin layer overlying the encrusted bright sands (Fig. 2C). These bright lines are linear ridges that separate the dark sands and have the same scale as the polygonal cracks.

Sequence and timing of events

On the basis of the contact between the bright and dark sand dunes and the localities of surficial structures (Figs. 1 and 2), we established the chronological order for the occurrence of the surficial geological processes observed. The bright barchan dunes were first formed during dry windblown events and then encrusted with sulfates/possibly chlorides as potential cementing agents in a more humid environment.

To constrain the ages of the bright barchan dunes, we identified 43 qualified craters (diameter, 2 to 9 m) on bright barchans based on the high-resolution remote sensing images (Materials and Methods). An age range of 1.4 to 0.4 million years (Ma; fig. S9) was acquired for the bright barchans using the chronology function (CF) model (21) and the impact crater production function (PF) (22). The ages determined for the bright barchans are within the range of ages (i.e., 3.0 to 0.1 Ma ago) for TARs from various regions from low to high latitudes (23).

Subsequently, cracks occurred on the surficial crusts of the bright dunes because of desiccation or freezing process. After that, the dark longitudinal dunes developed because of the late windblown event(s), followed by the formation of agglomerated particles on the surface of the dark sands. As a part of a circular region and a boundary between the bright and dark sands (Fig. 2, B and D), the bright strip-like trace may have formed later than the bright sands and even after the dark sands, probably synchronous with the formation of the agglomerated particles of the dark sands. The same is true for the chronological order of fragmented soil block and polygonal ridge (Fig. 2C) occurrences.

The sequence of events can be ordered (from old to young) as bright barchan dune formation; encrustation; cracking; dark sand deposition; and then lastly the latest events related to features including the agglomerated particles, the strip-like trace, the polygonal ridges, and the fragmented soil block. Superposition relationships show that all the observed surficial encrustation features are at most 1.4 Ma old and they might even be younger than 0.4 Ma old. Therefore, the stage when agglomerated particles, the polygonal ridges, the strip-like trace, and the fragmented soil block occurred was closest to the present.

DISCUSSION

Surficial cementation of soils forming so-called duricrusts has been widely observed at landing sites on Mars such as those of Spirit (24), Opportunity (25), and Curiosity (26). The duricrusts have thicknesses from a few millimeters up to 2 cm (27). Our inferred thickness of the bright sand crusts (i.e., 1.25 to 1.7 cm) at the Zhurong landing area is around the upper end of this range.

Sand surficial encrustation is not only a sign of the cessation of sand dune activity but also a precondition to forming cracks. This encrustation of dune surface can be attributed to the pore space between surficial sand grains being filled with cementing materials and agglutinating to form a whole body.

Possible cementing materials should be capable of transforming from gas/liquid to solid and filling pore spaces between sand grains. On the surface of Mars, candidate materials include dry ice, water ice, clays, salts, and other hydrated cementations (20, 28). On the basis of the properties of CO_2 and water (29) and the atmospheric conditions (30) at the Zhurong landing site, dry ice and water ice can be ruled out as cementing materials (Materials and Methods), at least on present-day Mars because both are not detected by LIBS. As mentioned, the SWIR data showed hydrous sulfates, opaline silica, ferric oxides, and probably chlorides in the sands (figs. S3 and S4). Therefore, sulfate-mixed salts and/or other hydrated cementations (i.e., opaline silica and ferric oxides), are the most likely materials for cementing the sand grains, although water ice may also have partially contributed to cementations. As recognized in previous studies, soil and soil crusts also have been thought to contain hydrated sulfate and opaline silica as cementing materials (31–33).

With salts and these hydrated materials as a cementing agent, the involvement of water is required. Water could originate from groundwater, thawed ice (snow or frost), or rainwater. Formation of an encrustation by evaporation of capillary water from groundwater is unlikely on a high-lying dune surface, whereas nearby low-

lying ground surfaces do not exhibit such cracks (fig. S1D). On the other hand, water can form on or fall to the ground in the form of either frost or rainwater/snow, respectively. Which mechanism is more likely depends on atmospheric temperature and vapor partial pressure on Mars.

As saturated vapor pressure is not related to atmospheric pressure but to temperature, which must reach 0°C (273 K) for vapor to condense into rainwater. Martian saturated water vapor pressure at 0°C is 611 Pa, accounting for ~72% of the observed atmospheric pressure (i.e., 786 to 834 Pa as determined by the Zhurong barometer). Such a percentage of water is impossible to attain considering that 95% of the modern atmosphere is CO_2 (34). Thus, rain on the present-day Mars is impossible.

On the basis of the atmospheric conditions determined by Zhurong, in combination with other ground-based observational data from Perseverance, InSight, and Curiosity, the inferred annual atmospheric temperature, pressure, and vapor partial pressure in the landing areas on Mars are between −105° and −5°C, from 683 to 849 Pa and 0.27 Pa, respectively (table S3 and fig. S10). At such conditions, the frost point is −74°C (199 K) (30). Therefore, water vapor can form as frost or snow in the landing area (Fig. 3), and frost/snow has been regarded as a common form of precipitation on Mars (35, 36).

Water frost/snow, if mixed with salts thereby lowering its melting point [i.e., from 205 to 271 K for sulfate-bearing salt mixture (table S4)], could thaw to become liquid saline water (table S4) (37, 38). As diurnal/seasonal temperature increases, frost/snow on the salt-bearing dune surfaces can start to sublimate because of reduced relative humidity (Fig. 3). If there is remanent frost/snow when temperature surpasses the saline water freezing point (i.e., eutectic temperature), then the frost/snow would thaw to form saline water. If temperature continues to rise, then saline water starts to vaporize and salts begins to precipitate to cement sand grains; thus, agglomerated particles could form, and crusts could eventually occur (Materials and Methods).

In the morning on Mars, atmospheric temperature experiences a rapid rise around 5:00 to 6:00 local true solar time (fig. S10D), which is conducive to the conversion of water from solid to liquid before all the frost/snow sublimates. Measured meteorological data (fig. S10, A and D) indicate that the temperature conditions for this conversion to occur can be met on both seasonal and diurnal time scales. The number of days for the annual occurrence of liquid water on Mars calculated according to the Ensemble Mars Atmosphere Reanalysis System (EMARS) dataset also supports the notion that liquid water could occur at the Zhurong landing area (fig. S11).

Orbital obliquity of Mars similar to or larger than the present-day angle has occurred repeatedly over the past 1.4 Ma (39), suggesting recurrence of comparable or more humid climatic and meteorological conditions than this modern period (40). Therefore, the
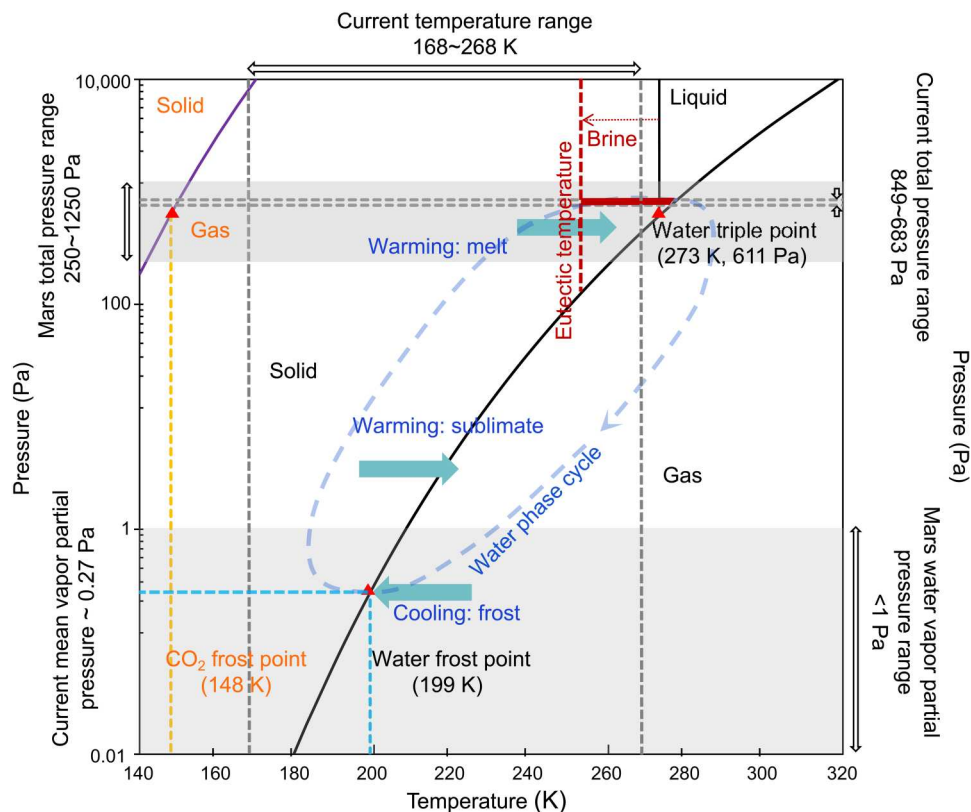

Fig. 3. Three-phase diagram showing conversion cycles of water (blue) and CO_2 (orange) under current Martian atmospheric condition. Saturated water vapor pressures (black line) at different temperatures were calculated on the basis of the amended Tetens formula. Saturated CO_2 vapor pressures (purple line) at various temperatures were obtained from the Clapeyron law. At the Zhurong landing site, the water frost point is ~199 K, and the water vapor partial pressure is 0.27 Pa (30). The CO_2 frost point is ~148 K (29); Martian atmospheric pressure ranges from 250 to 1250 Pa (16), and the range of Martian water vapor pressure is <1 Pa (71–73).

contemporary or even more humid climate permits the frequent occurrence of saline water at low latitudes on Mars.

In addition, acid ions in saline water in such aqueous process might favor extracting more Si from silicate minerals to form partially hydrated silica (especially Opal-CT) and other hydrated minerals, such as hydrated sulfate (bassanite and gypsum) and ferric oxides (especially ferrihydrite). Therefore, these geochemical weathering effects with aqueous process would improve the formation of agglomeration and encrustation on dune surface at the Zhurong landing site.

Surficial cracks usually occur because of the stress exerted on sediments during shrinkage due to desiccation or thermal contraction. When the associated stress becomes higher than the tensile strength of the sediments, fractures develop perpendicular to the direction of maximum tensile stress to produce polygonal cracks (41).

Polygonal cracks are also very common on Mars (19). However, there are only two categories of cracks associated with water. One type representing thermal contraction polygons are attributed to freeze-thaw cycles on Mars (19, 42–46). The other type represents polygonal cracks formed by desiccation (4, 7, 20). All reported water-associated cracks are either preserved in sedimentary horizons of early Mars (3, 4) or present on ground surfaces that are confined to mid-to-high latitudes and in the form of large-scale (>1 m) cracks (42–46) due to detecting techniques.

This study presents the first small-scale (centimeter scale) cracks formed on the salt-bearing encrustation of sand dunes at low latitudes. The cracks on the dune surfaces are most likely polygonal fractures caused by desiccation but not excluded to form by thermal contractions (table S2) when the rapid temperature change causes the saline water to freeze and shrink (8). Salt-cemented dune surfaces would become encrusted; then, during shrinkage, cracks could form under tensile stress.

The statistical morphological characteristics of cracks are in accordance with the parameters for desiccation polygonal cracks (table S2) with a centimeter-size scale rapidly formed when very homogeneous phyllosilicate- or salt-bearing materials experience intensive evaporation or diurnal thermal fluctuations (20). This comparison indicates that the even-textured salt-cementing bright sand surfaces could prompt cracks in the thin crust to develop because of rapid evaporation and/or seasonal/diurnal temperature variation.

At the interdune depression, we observe the strip-like trace, fragmented-soil block, and bright polygonal ridges on the surfaces of the sand dunes. These geomorphological phenomena could be related to meteorite impact, CO_2 frost processes, windblown processes, and water activity on the Martian surface.

Obviously, the strip-like trace and bright polygonal ridges are not related to meteorite impact. CO_2 frost processes have been proposed as a dry scenario to explain the formation of some slope features including recurring slope lineae and slope streaks (14, 47). However, they cannot account for any geomorphological features observed here because meteorological conditions exclude the presence of CO_2 frost at low latitudes (Materials and Methods).

As a part of the edge of a circular region, this bright strip-like trace at the bottom of an interdune depression has a round and smooth boundary (Fig. 2B), different in morphology and stretching characteristics from sand ripples on the bright barchan dunes (Fig. 1D). Moreover, no similar trace was observed on the surface of dark sands (Fig. 2B). These observations suggest that the strip-like trace may not be derived from wind activity but was a possible trace from aqueous process, such as thawed accumulative frost/snow.

In addition, the encrusted smooth bright sand surface, which has a higher reflectance factor (fig. S12) and mirror effect to reflect more heat back than dark sands, thus could serve as a cold trap to form much thicker, patchy, later frost/snow by recondensing water vapor from thin early frost/snow, which is similar to the cold trapping effect created by shadowing from small-scale surface roughness and troughs at the Viking 2 site (48). Therefore, a plausible scenario is accumulated frost/snow-thawed water on the circular bright sand crust of the left inclined region, leaving a dried trace of saline water in the circular slope region (Fig. 2F).

The fragmented-soil block may represent wind-eroded bedrock residues or ejecta resulting from meteorite impacts. However, the soil detritus only concentrates around the soil block, and no sands are found immediately outside the detritus pile. This observation is quite different in morphology from aeolian sands around rocks, which show continuous settlement from the surrounding sands on the ground (fig. S13). Thus, soil detritus around the soil block may not be related to meteorite impact or windblown deposition but to water-related fragmentation of the soil block, i.e., desiccation fracturing of the soil block after soaking in water. Because the soil detritus was naturally accumulated and not eroded by wind, they may have formed quite recently.

The bright polygonal ridges in another depression (Fig. 2C) also cannot be interpreted in terms of wind activity. They may represent salt deposition from saline water along polygonal cracks at the bottom of the depression, similar to that reported by a previous study (49), because of their similarity to polygonal cracks in morphology and scale and their positioning at the bottom of the interdune depression. As the bright polygonal ridges have influenced the dark sand distribution, they may have developed after dark sand deposition.

Collectively, these lines of evidence suggest that the cracks; crusts; agglomerated particles on dune surfaces; and the strip-like trace, fragmented soil block, polygonal ridges lying in the lowest part of the interdune depression were most likely associated with the activity of saline water, indicating the existence of water process on the low-latitude region of Mars. However, we should admit that some surficial morphological features (i.e., the polygonal ridges, the strip-like trace, and the fragmented soil block) are not very clear because of the limited image resolution. There may be other unexpected processes causing these features. It is necessary to perform careful observation during subsequent exploration.

In summary, we propose a hypothetical model for generating the crusts and cracks on the dune surfaces during the contemporary period (i.e., after 1.4 to 0.4 Ma ago). First, water vapor condensed as frost/snow on the dune surfaces when the temperature dropped below the frost point. Then, the frost/snow on salts in between the sand grains would thaw to eventually form saline water after the eutectic temperature was attained, and the saline water might accelerate the formation of hydrated silica and ferric oxides. Subsequently, the saline water would vaporize, and salts precipitate to cement sand grains as temperature reached above boiling point or low–water vapor content air flowed, thus agglomerating particles and forming crust. Then, continued drying or freezing would develop cracks within the crust. Last, repeated frost precipitation-thawing cycles could leave other traces related to water activity in the

interdune depression. Therefore, these crusts, cracks, and aggregates observed on the dune surfaces in Zhurong landing area provided the plausible evidence that saline water existed contemporarily at low latitudes on Mars.

If our water hypothesis is true, then the amount of water required to form crusts on dune surfaces and leave a trace of saline water is substantially higher than what has been discussed in terms of transient liquid water (i.e., thin films of water) in previous studies (50, 51). As reported, surface coatings on rocks and soil crusts on Mars were generated via acidic weathering of rocks with relatively limited water involvement (i.e., low water/rock ratio) and the geochemical effects of aqueous alteration involved in the formation of duricrusts; thus, rock surface coatings could accumulate over geologic time scales (52, 53). In contrast, aqueous activity accounting for surficial encrustation of sand dunes must have occurred in a short amount of time because relatively loose sand grains that have high mobility are unlikely to be cemented during a geologically slow process. In this case, more water seems to be required for cementing sand grains to form crusts, as compared with the duricrusts and rock surface coatings. This would imply that conditions more humid than expected in the past (and at high water vapor pressures) once existed after 1.4 to 0.4 Ma ago.

This theoretical feasibility of saline water in contemporary tropical latitudes on Mars is not unreasonable given the suspected large change in planetary obliquity since ca. 5 Ma ago (39). The scenario of changing axial tilt, establishing Mars current low-obliquity configuration only ca. 3 Ma ago, can explain the increased thickness of the polar ice caps in recent geological history as ice once abundant at lower latitudes during the past high-obliquity orbital configuration has been transferred to high latitudes under the current low-obliquity configuration (54). Our observation of water-related surface features may be associated with water vapor exchange between high and low latitudes over the past 1.4 Ma. Previous general circulation model (GCM) results also lend support to our water hypothesis by that there was enough liquid water at high obliquity excursions as erosive agent for gully formation (55). Thus, the discovery of vestigial saline water at low latitudes is consistent with models of recent Mars rotation (54, 56) and current understanding of the palaeoclimatic evolution of the polar ice caps (54).

Our findings provide useful clues for designing future exploration strategies for Mars rovers. Special attention should be paid to small depressions and encrusted soil surfaces, with the objective to look for more evidence of saline water to better understand contemporary climate changes at low latitudes on Mars. As saline water once existed at various latitudes on the surface of Mars, priority should be given to salt-tolerant microbes in future missions searching for extant life on Mars.

MATERIALS AND METHODS
Analysis of aggregates and crust at dune surface
The spatial resolution levels of the MSCam and the Micro-Imager (MI) onboard the Zhurong Mars rover are able to reach submillimeter and micrometer scales, allowing for observations of detailed morphological features of dune surfaces. The images from MSCam show that the coarse-grained aggregates (3 to 15 mm in diameter) are concentrated in the dark sand regions (figs. S1, C and E, and S2, B and C), forming a rough surface on the dune. By comparing the changes of dune surface material before and after LIBS hitting from MI images (fig. S2, B and C), we found that a lot of fine-grained material was produced in the pit of LIBS laser shot (LIBS crater). These fine-grained materials should have been created when the coarse grains or dune surface were crushed by the laser shock wave. These fine-grained materials vary in size from 0.1 to 0.3 mm, corresponding to fine sand (from 0.0125 to 0.25 mm), up to medium sand (from 0.25 to 0.5 mm) (57). Therefore, these coarse grains could represent aggregates of fine and medium sand grains not solid pebbles. There are less aggregates in bright sand regions, whose surfaces show layered and relatively smoothed crust structure (fig. S1, B and E). A similar scattering of fine and medium sand particles was also observed around the hole-like crater hit by the LIBS laser in the layered crust of a bright sand region (fig. S2F). For comparison, circular craters with a diameter of 0.3 mm were etched on the surface of quartzite (fig. S2, G to I) and on an onboard calibration target after ablation by LIBS, thus indicating that the crust surface where a larger hole-like crater formed is not completely solid but more likely cemented.

Evidence for cementing materials
Because the Zhurong landing site lies at 25°N, far from the northern polar ice cap, the temperature and pressure measured by the rover (table S3) could not allow CO_2 to be condensed to dry ice, where the necessary temperature is −148 K (29), at Martian atmospheric conditions. In addition, orbital observations at Mars (30) indicate that there is no visible CO_2 frost mantling at the landing site (fig. S10E). Therefore, dry ice is excluded from being the cementing material.

The atmospheric conditions during daytime when the rover was exploring sand dunes would not be expected to preserve water ice because the relatively high temperature would cause it to sublimate (Fig. 3). In this case, water ice could not be the main cementing material.

Observations on dark and bright sands were carried out using the MarSCoDe on Zhurong rover for Dunes 1, 2, and 3 by selecting two targets for each dune. MarSCoDe consists of a LIBS spectrometer (240 to 850 nm; resolution, >0.3 nm/pixel), SWIR spectrometer (850 to 2400 nm; resolution, >12 nm/pixel), and a micro-imager (58). The MarSCoDe suite was always calibrated by probing its onboard calibration targets before making scientific observations.

Surface reflectance spectra for Dunes 1 to 3 were obtained from corresponding SWIR level 2B data. For each observation, wavelength recalibration was first performed (59), original radiance was divided by the radiance of the onboard calibration targets captured during a temporally adjacent calibration and subsequently multiplied by a standard reflectance spectrum of the calibration targets analyzed in the laboratory on Earth to derive the reflectance spectrum from 850 to 2400 nm. The data were further smoothed by a sliding 15-pixel average filter and compared to the standard mineral spectrum in NASA Reflectance Experiment Laboratory Spectrum Library (60).

On fig. S3, it was noticed that the spectral features of the bright and dark sands among all the dunes exhibited a deep and broad absorption feature around 0.93 μm, which is mainly related to ferrous or ferric-rich minerals. Three distinct absorption features of hydrated minerals at ~1.46, ~1.95, and ~2.22 μm are shown in the SWIR spectra of dunes. The relatively weak absorption at ~1.46 μm is mainly caused by O─H stretching overtones and combinations (61), and the broad feature at ~1.95 μm resulted from combinations

of H—O—H bending and O—H stretching (*61*). The broad feature at ~2.22 µm is diagnostic of O—H stretching in hydrated silica (such as opal), aluminum clay (e.g., smectite), or hydrated sulfate (e.g., bassanite and gypsum) (*62–64*).

As shown in fig. S4, the absorption features of the hydrated silica (especially Opal-CT) and hydrated sulfate (especially bassanite, gypsum, hydroxylated Fe-sulfate, and starkeyite) are similar to those of dunes, with broad absorptions near ~1.95 and ~2.22 µm, and a good match of absorption near ~1.46 µm, indicating a high probability of containing these minerals in dunes. The Al-rich clay minerals also have an absorption feature near ~2.22 µm, but this absorption feature is narrower compared to that of dunes, and the absorption characteristics of Al-rich clay minerals at ~1.46 and ~1.95 µm are shifted to short wavelengths. In addition, the perchlorates and chlorides have significant absorption features at ~1.46 and ~1.95 µm, but the absorption feature at ~2.22 µm is not significant or absent in fig. S4 (H and I), suggesting that the presence of Al-rich clay, perchlorates, and chlorides on the dunes is uncertain.

For the absorption features of dunes at ~0.93 µm, we compared the features with that of the ferric oxides (e.g., hematite, ferrihydrite, goethite, and akaganeite). The features are similar to those of trivalent iron oxide minerals (especially ferrihydrite) at ~930 nm, and the absorption features of ferrihydrite at ~1.46 and ~1.95 µm are also in good agreement with that of the dunes.

The MarSCoDe LIBS Level 2B data were processed into continuous atomic spectra by ChemCam-style wavelet denoising (*65*), asymmetric least square (*62*), baseline extraction and removal, channels merging, and radiometric normalization. LIBS data also provided hints for the existence of hydrated sulfate and chloride salts. The major element compositions of bright and dark sand targets from Dune 1 were inferred from LIBS spectra through natural gradient boosting probabilistic prediction models (NGBoost) (*63*) trained from laboratory data. These predictions for major oxide concentrations are shown in table S1. The predicted total major oxide sums turned out to be far below 100%. The residual may be related to S, H, and Cl from all volatiles, including those from salts, some hydrated phases (i.e., ferric hydroxides), and amorphous phases that were not quantified by the model. Cl and S signal in these LIBS observations were unidentifiable, presumably because of their weak emissions below the noise level of the LIBS signals.

Under the present atmospheric conditions of Mars, sulfate minerals are able to absorb moisture from the atmosphere, leading to salt deliquescence, or they dissolve when meeting liquid water or ice. The resulting brines can act as adhesive agents that cement sand grains (*64*). Table S4 provides the eutectic temperatures of possible binary and ternary cryobrines on Mars, which range from 201 to 271 K. The eutectic temperature of the brine proposed in Fig. 3 falls into this range. According to the global distribution of a cemented sulfate endmember derived from Thermal Emission Spectrometer (TES) observations from Mars Global Surveyor (MGS) orbiter (fig. S6) (*66*), the landing site of Zhurong rover is located on the boundary between cemented and noncemented sulfates, which indicates the possible existence of cemented sulfate at the landing site. These considerations thus support the presence of sulfate-cemented agglomerates and crust on the dunes from additional perspectives.

Statistical analysis of crack parameters

On the basis of stereo image pairs obtained by the NaTeCam, the digital orthophoto map and digital elevation model for Dunes 2 and 3 are made using ContextCapture master (*67*). In the software, bundle adjustment was used to capture the optimized position and altitude of each NaTeCam image, and image-matching technique was applied to create a dense model for each stereo image pair. The root mean square error of the reprojection error for all the tie points is better than 0.3 pixels, which represent the accuracy of the terrain reconstruction of NaTeCam. The coordinate systems of these two data are east-north-up local Cartesian coordinates, and the origins are the same as the corresponding origins of the rover coordinate system. The readily identifiable cracks are manually drawn using vector editing tools of ArcMap (fig. S7, B to D and F). Parameters analyzed related to polygon properties include edge length, inner angle, edge number, and area. The edge length range and the area range of crack polygons are 0.3 to 13.5 cm (average = 4.8 cm) and 1.8 to 233.2 cm^2 (average = 55.2 cm^2), respectively (fig. S7, H and J). Such values represent the properties of small-scale fractures. These crack polygons mainly contain three to seven edges (fig. S7I), with inner angles ranging from 20° to 190° (average = 110°; fig. S7G), where Y-junctions are common. El-Maarry *et al.* (*20*) point out that if either rapid evaporation or appreciable diurnal heat fluctuation occurs at a homogenous surface, the joint points of fissures tend to become "Y" connected, where the angles around the joint would approach 120° rather than 90°, and the resulting shape of the polygons would typically be pentagonal or hexagonal with their edges less than 1 m in length. In addition, the cycle of crack formation and closure could be seasonal. Our statistical analysis of the cracks observed in Dunes 2 and 3 are consistent with such a scenario (*20*), where the cracks resulted from the subsequent desiccation of a thin and previously hydrated material.

Age dating of bright barchans

The crater size-frequency distribution method was used to acquire the absolute model ages of bright barchans within Zhurong landing site. On the basis of the derived 2262 dunes with a total area of ~0.45 km^2 in the 7 km–by–5 km dune statistical region, the CraterTools (*68*) on the ArcGIS platform was used to correctly extract craters superimposed on the dunes (fig. S8). During mapping craters, we tried to avoid the obvious secondary craters or crater chains and exclude the craters mantled by dunes. With the resolution improvement of remote sensing images, craters with diameters <10 m were used for dune dating (*23*). In this study, 43 effective craters (with diameters of 2 to 9 m) were identified and plotted in fig. S9. All the crater diameters are less than ~10 m, which is below the valid range of the CF model (*21*) and the impact crater PF model (*22*) on Mars. Therefore, we have drawn a series of isochrones of age using the CF model and PF model to analyze the upper and lower age limits of bright barchans, with reference to the age-limited method using isochrons by Reiss *et al.* (*69*). The frequency distribution of crater size with diameters less than ~2.7 m deviates from the isochrony. It may imply the last ending time of bright dunes being later than ~10 ka. Another possible reason is due to the limitation of the image resolution. Few craters with diameters less than ~2.7 m were observed, and the corresponding data points deviate from the overall trend. Thus, if they were excluded during the data analysis, the vast majority of the rest fall between 0.4- and 1.4-Ma isochrons,

suggesting that the best-fit model ages of bright barchans within Zhurong landing site ranges from ~0.4 to 1.4 Ma.

Atmospheric temperature, pressure, and humidity at the Zhurong landing site

The Mars Climate Station (MCS) installed on Zhurong can measure the temperature and pressure of the near-surface Martian atmosphere. During the first 9 months (So1s 10 to 256) of exploration, MCS was operational during each Martian solar day (sols) for only about 2 hours around noon, during which it acquired environmental data every 5 min. To analyze the maximum and minimum values of these discrete measurement data, the atmospheric temperature, pressure, and humidity results of Perseverance, InSight, and Curiosity were analyzed and compared (table S3).

During the 9-month exploration, the temperatures around noon at the Zhurong landing site ranged between −5° and −64°C. The measured sols covered those of the highest solar elevation at the landing site during a Martian year (fig. S10A). Therefore, it is estimated that the highest annual temperature at the landing site is about −5°C. Zhurong rover is located farther north than the InSight lander, which also landed in the northern hemisphere, so the lowest annual temperature at the Zhurong landing site is presumably lower than that of InSight (−105°C; fig. S10A).

The pressures around noon at the Zhurong landing site were between 675 and 853 Pa. According to the annual trends in meteorological data measured by Curiosity and InSight, a sine function is used to fit the annual variation of pressure (fig. S10B). Consequently, the annual variation range of pressure in the Zhurong landing area is about 683 to 849 Pa. The pressure model is given by following formula, which was established according to pressure values measured by MCS

$$P = 82.917 \times \sin(-2.959 \times 10^{-2} \times Ls + 27.939) + 766.170 \quad (1)$$

where Ls is solar longitude at Zhurong landing site and P is pressure value corresponding to Ls.

The maximum relative humidity measured by Curiosity during a Martian year was about 69%; thus, the maximum relative humidity at the Zhurong landing site could be higher considering its higher latitude. From the diurnal trends in temperature and humidity measured by Perseverance, InSight, and Curiosity (fig. S10D), the maximum relative humidity occurred when the temperatures became the lowest before dawn, around 5:00 to 6:00 in local true solar time. As the sun rose, the temperature would increase rapidly and could reach its maximum of the sol within a few Martian hours, resulting in the relative humidity in the near-surface atmosphere to decrease to a minimum.

Therefore, we take the annual temperature and air pressure ranges at the Zhurong landing site as ranging between −105° and −5°C and from 683 to 849 Pa, respectively, and the relative humidity should range from zero to greater than 69%. In addition, Khuller et al. (30) have calculated the global seasonal average water vapor abundance data and created a Martian global distribution map of average frost points of carbon dioxide and water (fig. S10, E and F). Figure S10F depicts the H_2O frost point at the Zhurong landing site, where the average water frost point is about −74°C (199 K). The average saturated water vapor partial pressure at the landing site is estimated as ~0.27 Pa using the modified Tetens

formula

$$E = 6.112 \times e^{17.67 \times \frac{t}{t+243.5}} \quad (2)$$

where $t = T − 273.15$ in °C, T is absolute temperature in K, and E is saturated water vapor partial pressure in hPa. The range of atmospheric temperature and pressure, as well as the estimated saturated water vapor partial pressure and frost point, at the landing site are summarized in table S3. We use the latest EMARS dataset containing gridded hourly atmospheric variables (70) to calculate the number of days during the Martian year that liquid water is likely to exist. Such days require two conditions: (i) a daily maximum surface temperature (T_{max}) exceeding 0°C and (ii) surface temperature and surface pressure above the triple point of water but below the boiling point. The Zhurong landing site is just located within the region where temperature and pressure are above the triple point, but below the boiling point, of H_2O (fig. S11). This further confirms the plausibility of the transient presence of liquid water in the Zhurong landing area during the contemporary period.

Reflectance factors of bright and dark sands

Raw MSCam images are processed through dark current removal, flat field correction, and radiometric calibration to convert observed digital number into physical radiance. Then, using near-in-time images of the MSCam calibration target, the solar irradiance reaching the Martian surface can be estimated, and thus, the reflectance factor of the images can be derived. The reflectance data as determined in eight wave bands of MSCam for bright sands are, by average, 12.5% higher than those of their adjacent dark sands (fig. S12). This discrepancy may be related to different composition and surface roughness. The relative high reflectance factor could make bright sands serve as a cold trap, which would recondense and redistribute the water vapor from thin early frost on surrounding dark sands and soils to form thicker, patchy, later frost on the surface of the bright sands.

Water phase changes on sand dune surfaces

On the basis of the estimated ranges of meteorological parameters at the Zhurong landing site, several stages of water phase transitions and their constraints could be determined (Fig. 3).

Cooling-frost/snow occurring stage

When the temperature drops below the frost point of water at the Zhurong landing site (−74°C or 199 K), water vapor becomes saturated so that frost/snow starts to form on the Martian surface. Frost/snow can form continuously within the range between −105° and −74°C.

Warming-sublimating stage

When the temperature increases and exceeds −74°C (199 K), the saturated vapor pressure of water increases, causing the relative humidity to decrease. During this time, frost/snow directly sublimates into water vapor, and sublimation continues until the temperature rises to the eutectic temperature (also the triple point of brine) of a mixture of ice and salts in the dunes.

Warming-melting stage

After the temperature exceeds the eutectic temperature of the mixture of ice and salts in the dune materials, at current Martian atmospheric pressure, the remaining frost/snow melts into saline water in the presence of salts in dune material. Liquid brine keeps forming until temperature rises to ~4°C or the ice is exhausted.

Warming-evaporating stage

While temperature rises above ~4°C, which is the gas-liquid equilibrium point of water under current Martian atmospheric pressure, continued warming would lower the partial pressure of water vapor to below the saturated vapor pressure, so that saline water begins to evaporate and transform into vapor and lastly disappears completely. The above water phase transition process would repeat again after entering the next cooling cycle.

Supplementary Materials

This PDF file includes:
Figs. S1 to S13
Tables S1 to S4
Data and materials description
References

Other Supplementary Material for this manuscript includes the following:
Data and materials

REFERENCES AND NOTES

1. T. M. Hoehler, An energy balance concept for habitability. *Astrobiology* **7**, 824–838 (2007).
2. S. W. Squyres, J. P. Grotzinger, R. E. Arvidson, J. F. Bell III, W. Calvin, P. R. Christensen, B. C. Clark, J. A. Crisp, W. H. Farrand, K. E. Herkenhoff, J. R. Johnson, G. Klingelhöfer, A. H. Knoll, S. M. McLennan, H. Y. McSween Jr., R. V. Morris, J. W. Rice Jr., R. Rieder, L. A. Soderblom, In situ evidence for an ancient aqueous environment at Meridiani Planum, Mars. *Science* **306**, 1709–1714 (2004).
3. S. M. McLennan, J. F. Bell III, W. M. Calvin, P. R. Christensen, B. C. Clark, P. A. de Souza, J. Farmer, W. H. Farrand, D. A. Fike, R. Gellert, A. Ghosh, T. D. Glotch, J. P. Grotzinger, B. Hahn, K. E. Herkenhoff, J. A. Hurowitz, J. R. Johnson, S. S. Johnson, B. Jolliff, G. Klingelhöfer, A. H. Knoll, Z. Learner, M. C. Malin, H. Y. McSween Jr., J. Pocock, S. W. Ruff, L. A. Soderblom, S. W. Squyres, N. J. Tosca, W. A. Watters, M. B. Wyatt, A. Yen, Provenance and diagenesis of the evaporite-bearing Burns formation, Meridiani Planum, Mars. *Earth Planet. Sci. Lett.* **240**, 95–121 (2005).
4. J. Grotzinger, J. Bell III, K. Herkenhoff, J. Johnson, A. Knoll, E. McCartney, S. McLennan, J. Metz, J. Moore, S. Squyres, R. Sullivan, O. Ahronson, R. Arvidson, B. Joliff, M. Golombek, K. Lewis, T. Parker, J. Soderblom, Sedimentary textures formed by aqueous processes, Erebus crater, Meridiani Planum, Mars. *Geology* **34**, 1085–1088 (2006).
5. D. W. Ming, D. W. Mittlefehldt, R. V. Morris, D. C. Golden, R. Gellert, A. Yen, B. C. Clark, S. W. Squyres, W. H. Farrand, S. W. Ruff, R. E. Arvidson, G. Klingelhöfer, H. Y. McSween, D. S. Rodionov, C. Schröder, P. A. de Souza Jr., A. Wang, Geochemical and mineralogical indicators for aqueous processes in the Columbia Hills of Gusev crater, Mars. *J. Geophys. Res.* **111**, E02S12 (2006).
6. M. Nachon, S. M. Clegg, N. Mangold, S. Schröder, L. C. Kah, G. Dromart, A. Ollila, J. R. Johnson, D. Z. Oehler, J. C. Bridges, S. Le Mouélic, O. Forni, R. C. Wiens, R. B. Anderson, D. L. Blaney, J. F. Bell III, B. Clark, A. Cousin, M. D. Dyar, B. Ehlmann, C. Fabre, O. Gasnault, J. Grotzinger, J. Lasue, E. Lewin, R. Léveillé, S. McLennan, S. Maurice, P.-Y. Meslin, W. Rapin, M. Rice, S. W. Squyres, K. Stack, D. Y. Sumner, D. Vaniman, D. Wellington, Calcium sulfate veins characterized by ChemCam/Curiosity at Gale crater, Mars. *J. Geophys. Res.* **119**, 1991–2016 (2014).
7. N. Stein, J. P. Grotzinger, J. Schieber, N. Mangold, B. Hallet, H. Newsom, K. M. Stack, J. A. Berger, L. Thompson, K. L. Siebach, A. Cousin, S. Le Mouélic, M. Minitti, D. Y. Sumner, C. Fedo, C. H. House, S. Gupta, A. R. Vasavada, R. Gellert, R. C. Wiens, J. Frydenvang, O. Forni, P. Y. Meslin, V. Payré, E. Dehouck, Desiccation cracks provide evidence of lake drying on Mars, Sutton Island member, Murray formation, Gale Crater. *Geology* **46**, 515–518 (2018).
8. R. D. Wordsworth, The climate of early Mars. *Annu. Rev. Earth Planet. Sci.* **44**, 381–408 (2016).
9. A. P. Ingersoll, Mars: Occurrence of liquid water. *Science* **168**, 972–973 (1970).
10. M. H. Hecht, Metastability of liquid water on Mars. *Icarus* **156**, 373–386 (2002).
11. N. O. Rennó, B. J. Bos, D. Catling, B. C. Clark, L. Drube, D. Fisher, W. Goetz, S. F. Hviid, H. U. Keller, J. F. Kok, S. P. Kounaves, K. Leer, M. Lemmon, M. B. Madsen, W. J. Markiewicz, J. Marshall, C. McKay, M. Mehta, M. Smith, M. P. Zorzano, P. H. Smith, C. Stoker, S. M. M. Young, Possible physical and thermodynamical evidence for liquid water at the Phoenix landing site. *J. Geophys. Res.* **114**, E00E03 (2009).
12. A. S. McEwen, L. Ojha, C. M. Dundas, S. S. Mattson, S. Byrne, J. J. Wray, S. C. Cull, S. L. Murchie, N. Thomas, V. C. Gulick, Seasonal flows on warm Martian slopes. *Science* **333**, 740–743 (2011).
13. M. C. Malin, K. S. Edgett, Evidence for recent groundwater seepage and surface runoff on Mars. *Science* **288**, 2330–2335 (2000).
14. C. M. Dundas, Dry formation of recent Martian slope features, in *Mars Geological Enigmas from the Late Noachian Epoch to the Present Day*, R. Soare, S. Conway, J.-P. Williams, D. Oehler, Eds. (Elsevier, 2021), pp. 263–288.
15. S. J. Conway, D. E. Stillman, The role of liquid water in recent surface processes on Mars, in *Mars Geological Enigmas from the Late Noachian Epoch to the Present Day*, R. Soare, S. Conway, J.-P. Williams, D. Oehler, Eds. (Elsevier, 2021), pp. 207–261.
16. R. M. Haberle, C. P. McKay, J. Schaeffer, N. A. Cabrol, E. A. Grin, A. P. Zent, R. Quinn, On the possibility of liquid water on present-day Mars. *J. Geophys. Res.* **106**, 23317–23326 (2001).
17. K. L. Tanaka, J. A. Skinner Jr., J. M. Dohm, R. P. Irwin, III, E. J. Kolb, C. M. Fortezzo, T. Platz, G. G. Michael, T. M. Hare, *Geological Map of Mars* (Scientific Investigations Map 3292, USGS, 2014).
18. J. Liu, R. Zhang, W. Rao, X. Cui, Y. Geng, Y. Jia, H. Huang, X. Ren, W. Yan, X. Zeng, W. Wen, X. Wang, X. Gao, Q. Fu, Y. Zhu, J. Dong, H. Li, X. Wang, W. Zuo, Y. Su, D. Kong, H. Zhang, Geomorphic contexts and science focus of the Zhurong landing site on Mars. *Nat. Astron.* **6**, 65–71 (2022).
19. J. Levy, J. Head, D. Marchant, Thermal contraction crack polygons on Mars: Classification, distribution, and climate implications from HiRISE observations. *J. Geophys. Res.* **114**, E01007 (2009).
20. M. R. El-Maarry, W. Watters, N. K. McKeown, J. Carter, E. N. Dobrea, J. L. Bishop, A. Pommerol, N. Thomas, Potential desiccation cracks on Mars: A synthesis from modeling, analogue-field studies, and global observations. *Icarus* **241**, 248–268 (2014).
21. B. A. Ivanov, Mars/Moon cratering rate ratio estimates. *Space Sci. Rev.* **96**, 87–104 (2001).
22. W. K. Hartmann, G. Neukum, Cratering chronology and the evolution of Mars. *Space Sci. Rev.* **96**, 165–194 (2001).
23. D. C. Berman, M. R. Balme, S. C. R. Rafkin, J. R. Zimbelman, Transverse Aeolian Ridges (TARs) on Mars II: Distributions, orientations, and ages. *Icarus* **213**, 116–130 (2011).
24. R. Arvidson, R. C. Anderson, P. Bartlett, J. F. Bell III, D. Blaney, P. R. Christensen, P. Chu, L. Crumpler, K. Davis, B. L. Ehlmann, R. Fergason, M. P. Golombek, S. Gorevan, J. A. Grant, R. Greeley, E. A. Guinness, A. F. C. Haldemann, K. Herkenhoff, J. Johnson, G. Landis, R. Li, R. Lindemann, H. McSween, D. W. Ming, T. Myrick, L. Richter, F. P. Seelos IV, S. W. Squyres, R. J. Sullivan, A. Wang, J. Wilson, Localization and physical properties experiments conducted by spirit at Gusev crater. *Science* **305**, 821–824 (2004).
25. K. Herkenhoff, S. W. Squyres, R. Arvidson, D. S. Bass, J. F. Bell III, P. Bertelsen, B. L. Ehlmann, W. Farrand, L. Gaddis, R. Greeley, J. Grotzinger, A. G. Hayes, S. F. Hviid, J. R. Johnson, B. Jolliff, K. M. Kinch, A. H. Knoll, M. B. Madsen, J. N. Maki, S. M. McLennan, H. Y. McSween, D. W. Ming, J. W. Rice Jr., L. Richter, M. Sims, P. H. Smith, L. A. Soderblom, N. Spanovich, R. Sullivan, S. Thompson, T. Wdowiak, C. Weitz, P. Whelley, Evidence from opportunity's microscopic imager for water on Meridiani planum. *Science* **306**, 1727–1730 (2004).
26. D. F. Blake, R. V. Morris, G. Kocurek, S. M. Morrison, R. T. Downs, D. Bish, D. W. Ming, K. S. Edgett, D. Rubin, W. Goetz, M. B. Madsen, R. Sullivan, R. Gellert, I. Campbell, A. H. Treiman, S. M. McLennan, A. S. Yen, J. Grotzinger, D. T. Vaniman, S. J. Chipera, C. N. Achilles, E. B. Rampe, D. Sumner, P.-Y. Meslin, S. Maurice, O. Forni, O. Gasnault, M. Fisk, M. Schmidt, P. Mahaffy, L. A. Leshin, D. Glavin, A. Steele, C. Freissinet, R. Navarro-González, R. A. Yingst, L. C. Kah, N. Bridges, K. W. Lewis, T. F. Bristow, J. D. Farmer, J. A. Crisp, E. M. Stolper, D. J. Des Marais, P. Sarrazin; MSL Science Team, Curiosity at Gale crater, Mars: Characterization and analysis of the Rocknest sand shadow. *Science* **341**, 1239505 (2013).
27. N. Kömle, C. Pitcher, Y. Gao, L. Richter, Study of the formation of duricrusts on the Martian surface and their effect on sampling equipment. *Icarus* **281**, 220–227 (2017).
28. S. R. Taylor, S. McLennan, *Planetary Crusts: Their Composition, Origin and Evolution* (Cambridge Univ. Press, 2009).
29. S. Piqueux, A. Kleinböhl, P. O. Hayne, N. G. Heavens, D. M. Kass, D. J. McCleese, J. T. Schofield, J. H. Shirley, Discovery of a widespread low-latitude diurnal CO2 frost cycle on Mars. *J. Geophys. Res.* **121**, 1174–1189 (2016).
30. A. R. Khuller, P. R. Christensen, T. N. Harrison, S. Diniega, The distribution of frosts on Mars: Links to present-day gully activity. *J. Geophys. Res.* **126**, e2020JE006577 (2021).
31. R. Sharp, M. Malin, Surface geology from viking landers on Mars: A second look. *Geol. Soc. Am. Bull.* **95**, 1398–1412 (1984).
32. C. D. Cooper, J. F. Mustard, Spectroscopy of loose and cemented sulfate-bearing soils: Implications for duricrust on Mars. *Icarus* **158**, 42–55 (2002).
33. Y. Liu, X. Wu, Y. Y. Zhao, P. Lu, C. Wang, J. Liu, Z. X. Zhao, X. Zhou, C. L. Zhang, Y. C. Wu, W. H. Wan, Y. L. Zou, Zhurong reveals recent aqueous activities in Utopia Planitia, Mars. *Sci. Adv.* **8**, eabn8555 (2022).
34. G. P. Kuiper, *The Atmospheres of the Earth and Planets* (University of Chicago Press, 1952).

35. F. G. Carrozzo, G. Bellucci, F. Altieri, E. D'Aversa, J.-P. Bibring, Mapping of water frost and ice at low latitudes on Mars. *Icarus* **203**, 406–420 (2009).

36. M. Vincendon, F. Forget, J. Mustard, Water ice at low to midlatitudes on Mars. *J. Geophys. Res.* **115**, E10001 (2010).

37. R. V. Gough, V. F. Chevrier, K. J. Baustian, M. E. Wise, M. A. Tolbert, Laboratory studies of perchlorate phase transitions: Support for metastable aqueous perchlorate solutions on Mars. *Earth Planet. Sci. Lett.* **312**, 371–377 (2011).

38. E. Fischer, G. M. Martínez, H. M. Elliott, N. O. Rennó, Experimental evidence for the formation of liquid saline water on Mars. *Geophys. Res. Lett.* **41**, 4456–4462 (2014).

39. J. Laskar, B. Levrard, J. F. Mustard, Orbital forcing of the Martian polar layered deposits. *Nature* **419**, 375–377 (2002).

40. M. T. Mellon, B. M. Jakosky, Geographic variations in the thermal and diffusive stability of ground ice on Mars. *J. Geophys. Res.* **98**, 3345–3364 (1993).

41. K. A. Shorlin, J. R. de Bruyn, M. Graham, S. W. Morris, Development and geometry of isotropic and directional shrinkage-crack patterns. *Phys. Rev. E.* **61**, 6950–6957 (2000).

42. M. T. Mellon, Small-scale polygonal features on Mars: Seasonal thermal contraction cracks in permafrost. *J. Geophys. Res.* **102**, 25617–25628 (1997).

43. D. R. Marchant, J. W. Head III, Antarctic Dry Valleys: Microclimate zonation, varia-ble geomorphic processes, and implications for assessing climate change on Mars. *Icarus* **192**, 187–222 (2007).

44. N. M. Seibert, J. S. Kargel, Small-scale Martian polygonal terrain: Implications for liquid surface water. *Geophys. Res. Lett.* **28**, 899–902 (2001).

45. N. Mangold, High latitude patterned grounds on Mars: Classification, distribution and climatic control. *Icarus* **174**, 336–359 (2005).

46. A. Lefort, P. S. Russell, N. Thomas, A. S. McEwen, C. M. Dundas, R. L. Kirk, Observations of periglacial landforms in Utopia Planitia with the High Resolution Imaging Science Experiment (HiRISE). *J. Geophys. Res.* **114**, E04005 (2009).

47. L. H. Lark, C. Huber, J. W. Head, Anomalous recurring slope lineae on Mars: Implications for formation mechanisms. *Icarus* **357**, 114129 (2021).

48. T. Svitek, B. Murray, Winter frost at Viking Lander 2 site. *J. Geophys. Res.* **95**, 1495–1510 (1990).

49. G. V. Chavdarian, D. Y. Sumner, Cracks and fins in sulfate sand: Evidence for recent mineral-atmospheric water cycling in Meridiani Planum outcrops? *Geology* **34**, 229–232 (2006).

50. D. T. F. Möhlmann, Water in the upper Martian surface at mid- and low-latitudes: presence, state, and consequences. *Icarus* **168**, 318–323 (2004).

51. C. S. Boxe, K. P. Hand, K. H. Nealson, Y. L. Yung, A. S. Yen, A. Saiz-Lopez, Adsorbed water and thin liquid films on Mars. *Int. J. Astrobiol.* **11**, 169–175 (2012).

52. L. A. Haskin, A. Wang, B. L. Jolliff, H. Y. McSween, B. C. Clark, D. J. Des Marais, S. M. McLennan, N. J. Tosca, J. A. Hurowitz, J. D. Farmer, A. Yen, S. W. Squyres, R. E. Arvidson, K. Klingelhöfer, C. Schröder, P. A. de Souza Jr., D. W. Ming, R. Gellert, J. Zipfel, J. Brückner, J. F. Bell III, K. Herkenhoff, P. R. Christensen, S. Ruff, D. Blaney, S. Gorevan, N. A. Cabrol, L. Crumpler, J. Grant, L. Soderblom, Water alteration of rocks and soils on Mars at the Spirit rover site in Gusev crater. *Nature* **436**, 66–69 (2005).

53. J. A. Hurowitz, S. M. McLennan, N. J. Tosca, R. E. Arvidson, J. R. Michalski, D. W. Ming, C. Schröder, S. W. Squyres, In situ and experimental evidence for acidic weathering of rocks and soils on Mars. *J. Geophys. Res.* **111**, E02S19 (2006).

54. B. Levrard, F. Forget, F. Montmessin, J. Laskar, Recent formation and evolution of northern Martian polar layered deposits as inferred from a Global Climate Model. *J. Geophys. Res.* **112**, E06012 (2007).

55. J. L. Dickson, L. Kerber, C. I. Fassett, J. W. Head, F. Forget, J.-B. Madeleine, Formation of Gullies on Mars by Water at High Obliquity: Quantitative Integration of Global Climate Models and Gully Distribution, 46th Lunar and Planetary Science Conference, Abstract #1035, 2015.

56. C. Leovy, Weather and climate on Mars. *Nature* **412**, 245–249 (2001).

57. C. K. Wentworth. A scale of grade and class terms for clastic sediments. *J. Geol.* **30**(5), 377–392 (1922).

58. W. Xu, X. Liu, Z. Yan, L. Li, Z. Zhang, Y. Kuang, H. Jiang, H. Yu, F. Yang, C. Liu, T. Wang, C. Li, Y. Jin, J. Shen, B. Wang, W. Wan, J. Chen, S. Ni, Y. Ruan, R. Xu, C. Zhang, Z. Yuan, X. Wan, Y. Yang, Z. Li, Y. Shen, D. Liu, B. Wang, R. Yuan, T. Bao, R. Shu, The MarSCoDe instrument suite on the Mars Rover of China's Tianwen-1 mission. *Space Sci. Rev.* **217**, 64 (2021).

59. X. Tan, J. Liu, X. Zhang, W. Yan, W. Chen, X. Ren, W. Zuo, C. Li, Design and validation of the scientific data products for China's Tianwen-1 mission. *Space Sci. Rev.* **217**, 69 (2021).

60. C. E. Viviano-Beck, *et al.*, MRO CRISM Type Spectra Library, NASA Planetary Data System (2015); https://crismtypespectra.rsl.wustl.edu.

61. C. Li, D. Liu, B. Liu, X. Ren, J. Liu, Z. He, W. Zuo, X. Zeng, R. Xu, X. Tan, X. Zhang, W. Chen, R. Shu, W. Wen, Y. Su, H. Zhang, Z. Ouyang, Chang'E-4 initial spectroscopic identification of lunar far-side mantle-derived materials. *Nature* **569**, 378–382 (2019).

62. P. H. C. Eilers, A perfect smoother. *Anal. Chem.* **75**, 3631–3636 (2003).

63. T. Duan, A. Avati, D. Y. Ding, S. Basu, A. Ng, A. Schuler, NGBoost: Natural Gradient Boosting for Probabilistic Prediction, paper presented at the Proceedings of the 37th International Conference on Machine Learning, Virtual, 13 to 18 July 2020. p. 2690–2700.

64. B. C. Clark, D. C. Van Hart, The salts of Mars. *Icarus* **45**, 370–378 (1981).

65. R. Wiens, S. Maurice, J. Lasue, O. Forni, R. B. Anderson, S. Clegg, S. Bender, D. Blaney, B. L. Barraclough, A. Cousin, L. Deflores, D. Delapp, M. D. Dyar, C. Fabre, O. Gasnault, N. Lanza, J. Mazoyer, N. Melikechi, P.-Y. Meslin, H. Newsom, A. Ollila, R. Perez, R. L. Tokar, D. Vaniman, Pre-flight calibration and initial data processing for the ChemCam laser-induced breakdown spectroscopy instrument on the Mars Science Laboratory Rover. *Spectrochim. Acta Part B At. Spectrosc.* **82**, 1–27 (2013).

66. C. D. Cooper, J. F. Mustard, TES observations of the global distribution of sulfate on Mars, in *32nd Lunar and Planetary Science Conference* (Lunar and Planetary Institute, 2001), pp. 2048.

67. J. Liu, X. Ren, W. Yan, C. Li, H. Zhang, Y. Jia, X. Zeng, W. Chen, X. Gao, D. Liu, X. Tan, X. Zhang, T. Ni, H. Zhang, W. Zuo, Y. Su, W. Wen, Descent trajectory reconstruction and landing site positioning of Chang'E-4 on the lunar farside. *Nat. Commun.* **10**, 4229 (2019).

68. T. Kneissl, S. van Gasselt, G. Neukum, Map-projection-independent crater size-frequency determination in GIS environments—New software tool for ArcGIS. *Planet. Space Sci.* **59**, 1243–1254 (2011).

69. D. Reiss, S. van Gasslet, G. Neukum, R. Jaumann, Absolute dune ages and implications for the time of formation of gullies in Nirgal Vallis, Mars. *J. Geophys. Res.* **109**, E06007 (2004).

70. S. J. Greybush, E. Kalnay, R. J. Wilson, R. N. Hoffman, T. Nehrkorn, M. Leidner, J. Eluszkiewicz, H. E. Gillespie, M. Wespetal, Y. Zhao, M. Hoffman, P. Dudas, T. McConnochie, A. Kleinböhl, D. Kass, D. McCleese, T. Miyoshi, The Ensemble Mars Atmosphere Reanalysis System (EMARS) Version 1.0. *Geosci. Data J.* **6**, 137–150 (2019).

71. A. P. Zent, M. H. Hecht, D. R. Cobos, S. E. Wood, T. L. Hudson, S. M. Milkovich, L. P. DeFlores, M. T. Mellon, Initial results from the thermal and electrical conductivity probe (TECP) on Phoenix. *J. Geophys. Res.* **115**, E00E14 (2010).

72. E. Jones, C. Lineweaver, Using the phase diagram of liquid water to search for life. *Aust. J. Earth Sci.* **59**, 253–262 (2012).

73. H. Savijärvi, A. Määttänen, Boundary-layer simulations for the Mars *Phoenix* lander site. *Q. J. Roy. Meteorol. Soc.* **136**, 1497–1505 (2010).

74. D. Möhlmann, K. Thomsen, Properties of cryobrines on Mars. *Icarus* **212**, 123–130 (2011).

75. G. W. Brass, Stability of brines on Mars. *Icarus* **42**, 20–28 (1980).

76. V. F. Chevrier, T. S. Altheide, Low temperature aqueous ferric sulfate solutions on the surface of Mars. *Geophys. Res. Lett.* **35**, L22101 (2008).

77. V. F. Chevrier, J. Hanley, T. S. Altheide, Stability of perchlorate hydrates and their liquid solutions at the Phoenix landing site, Mars. *Geophys. Res. Lett.* **36**, L10202 (2009).

78. E. Usdowski, M. Dietzel, *Atlas and Data of Solid-Solution Equilibria of Marine Evaporites* (Springer, 1998)

79. N. K. Voskresenskaya, O. K. Yanat'eva, Equilibria in the system: Water-lithium chloride-ammonium chloride. *Izv. Sekt. Fiz-Khim. Anal.* **9**, 291–293 (1936).

80. W. F. Linke, A. Seidell, *Solubilities of Inorganic and Metal-Organic Compounds* (American Chemical Society, 1965).